Proximity-induced chiral quantum light generation in strain-engineered WSe2/NiPS3 heterostructures

Htoon, Han
Jones, Andrew Crandall
Choi, Junho
Zhao, Huan
Chandrasekaran, Vigneshwaran
Pettes, Michael Thompson
Piryatinski, Andrei
Sinitsyn, Nikolai
Crooker, Scott A.
Li, Xiangzhi

To be published in: Nature Materials

DOI to publisher's version: 10.1038/s41563-023-01645-7

Proximity-induced chiral quantum light generation in strain-engineered $WSe_2/NiPS_3$ heterostructures

Xiangzhi Li[1], Andrew C. Jones[1], Junho Choi[1], Huan Zhao[1], Vigneshwaran Chandrasekaran[1], Michael T. Pettes[1], Andrei Piryatinski[1], Märta A. Tschudin[2], Patrick Reiser[2], David A. Broadway[2], Patrick Maletinsky[2], Nikolai Sinitsyn[1], Scott A. Crooker[1] & Han Htoon[1]

[1]Los Alamos National Laboratory, Los Alamos, NM, USA
[2]Department of Physics, University of Basel, Basel, Switzerland

Abstract
Quantum light emitters capable of generating single photons with circular polarization and non-classical statistics could enable non-reciprocal single-photon devices and deterministic spin–photon interfaces for quantum networks. To date, the emission of such chiral quantum light relies on the application of intense external magnetic fields, electrical/optical injection of spin-polarized carriers/excitons or coupling with complex photonic metastructures. Here we report the creation of free-space chiral quantum light emitters via the nanoindentation of monolayer $WSe_2/NiPS_3$ heterostructures at zero external magnetic field. These quantum light emitters emit with a high degree of circular polarization (0.89) and single-photon purity (95%), independent of pump laser polarization. Scanning diamond nitrogen-vacancy microscopy and temperature-dependent magneto-photoluminescence studies reveal that the chiral quantum light emission arises from magnetic proximity interactions between localized excitons in the WSe_2 monolayer and the out-of-plane magnetization of defects in the antiferromagnetic order of $NiPS_3$, both of which are co-localized by strain fields associated with the nanoscale indentations.

Main

Defined as the process by which an atomically thin material acquires properties from adjacent materials via quantum mechanical interactions, proximity effects have recently emerged as a means of inducing desirable magnetic, topological, transport and optical properties in two-dimensional (2D) systems[1,2,3]. Strong enhancements in valley Zeeman splitting[4,5] and spin-dependent charge transfer[6,7,8,9] have been observed through the coupling of semiconducting transition metal dichalcogenide (TMD) monolayers to magnetic thin films (for example, EuS)[4] and van der Waals magnets (for example, CrI_3 (refs. 8,9,10), $CrBr_3$ (refs. 6,7), $Cr_2Ge_2Te_2$ (ref. 5) and Fe_3GeTe_2 (ref. 11)). The inverse proximity effect where TMD monolayer altering 2D magnetic materials through spin–orbit coupling has also been reported[12]. However, few studies have focused on exploiting proximity effects to manipulate the chirality of quantum emitters (QEs) in monolayer TMDs[5,8,11]. To date, such manipulations demand the application of external magnetic fields[13,14], injection of spin-polarized carriers/excitons[2,15,16,17] or coupling with complex photonic metastructures[18,19].

In parallel, the studies of transition metal phosphorous trichalcogenide $TMPX_3$ (TM = Mn, Ni, Fe, Co; X = S, Se) van der Waals antiferromagnetic (AFM) crystals have recently opened new frontiers for exploring 2D magnetism with applications in spintronic and quantum information technologies[20]. Recent breakthroughs include the discovery of charge–spin correlation[21], the spin-induced linear polarization of excitons[22,23,24] and the switching of the Néel vector under strain[25]. The potential of these materials to support magnons, which are the collective excitation of local magnetic moments[26], as a means of coupling QEs represents an additional opportunity for the realization of microwave–magnon–spin quantum interfaces[27]. Still, the study of whether $TMPX_3$ materials are capable of modifying the properties of free and localized excitons in 2D TMD materials via the proximity effect remains in its nascent stage[28]. Here we show that $WSe_2/NiPS_3$ heterostructures locally strained via nanoindentations[29] can support QEs capable of emitting single photons with strong circular polarization at zero magnetic field and independent of excitation polarization. This observation is surprising because $NiPS_3$ displays AFM order[26], and is therefore not expected to yield a net out-of-plane magnetization capable of enhancing the valley Zeeman effect and thus induce circularly polarized photoluminescence (PL). This finding could be exploited in the development of non-reciprocal single-photon devices and deterministic spin–photon interfaces[18,19] for quantum networks.

Circularly polarized PL at zero magnetic field

Figure 1a–c displays a representative heterostructure consisting of an ~50-nm-thick $NiPS_3$ flake and a monolayer-thick WSe_2 flake stacked atop a Si wafer coated with a 300-nm-thick polymer layer. Wide-field PL images acquired at cryogenic temperatures (T = 4 K) under 514 nm continuous-wave laser excitation (Fig. 1b) show that PL from the WSe_2 monolayer is strongly quenched when coupled to $NiPS_3$. The PL spectra acquired from unstrained regions R1 and R2 showed no degree of circular polarization (DCP), indicating that electron–hole pairs preferentially pumped non-resonantly into the K^+ valley relax equally to both valleys before recombination (Extended Data Fig. 2). Next, localized QEs on the heterostructure were created using strain engineering[29] by pressing a blunt atomic force microscopy probe (~100 nm radius of curvature) into the heterostructure to form an array of nanoindentations measuring ~250 nm in diameter, 175 nm in depth and surrounded by an ~100-nm-high circular ridge (Fig. 1c). Bright localized PL emission with spectrally narrow peaks is observed at indentation locations (Fig. 1d–f)[29]. In contrast to the unpolarized PL emission of narrow peaks reported on WSe_2 monolayer on polymethyl methacrylate (PMMA)[29] and hexagonal boron nitride (Extended Data Fig. 3a), we observed clear, circularly polarized PL from some of the sharp emission peaks under linearly polarized laser excitation at zero magnetic field (Fig. 1d–f). This circularly polarized emission behaviour was also observed to remain unchanged when the excitation laser polarization is changed to σ^+, σ^- or linear polarization of different orientations (Extended Data Fig. 3b,c). Both polarity and DCP ($(I_{\sigma+} - I_{\sigma-})/(I_{\sigma+} + I_{\sigma-})$) vary widely among the localized PL emission peaks. Some indented spots display multiple localized peaks with opposite circular polarizations (Fig. 1d). An analysis of the spectral image of sharp PL peaks from an

individual indentation (Extended Data Fig. 4) reveals that these sharp PL peaks originate from independent localized exciton states separated by 50 to a few hundred nanometres. Also, σ^+ and σ^- peaks of all the localized emitters were found to occur at identical energies. Localized emitters also exhibit weak linear polarization (Extended Data Fig. 5a,b) with zero energy splitting between the two components. Based on these observations, we attribute the σ^+ and σ^- PL peaks of localized emitters to the emission of a single-exciton state exhibiting a strong but incomplete DCP. The chiral emission peaks are observed in the same 1.5–1.7 eV range as in the case of strain-engineered WSe_2 monolayers[30] with linewidths of 3.6 ± 1.3 meV (Extended Data Fig. 5c), broader than the sharpest linewidths reported[30], but comparable with those formed via nanoindentations[29] and those induced via strain on the edge of SiN photonic waveguides[31].

Chiral quantum light emission

To demonstrate the capability of chiral emission sites to act as QEs, we performed Hanbury Brown–Twiss experiments. Figure 2a,b shows circular-polarization-resolved PL spectra recorded from an indentation excited with either σ^+ and σ^- polarization, respectively. Spectrally filtering the lowest-energy peak (E = 1.629 eV, DCP = –0.3) showing strong σ^- polarization, we next acquired the intensity versus time trace, decay curve and second-order photon correlation function ($g^{(2)}(\tau)$) of the PL (Methods). The PL intensity versus time trace (Fig. 2c) shows blinking-free emission, whereas the decay curve (Fig. 2d) can be fitted to a single exponential with a lifetime of 4.35 ± 0.01 ns. Ultimately, the $g^{(2)}$ trace (Fig. 2e) provides clear evidence of quantum light emission such that for more than 80% of the time, the QE emits a single photon per excitation–emission cycle (meaning single-photon purity of 80%) comparable with other reported WSe_2 QEs[30]. We attribute the residual multiphoton emission probability ($g^{(2)}(0)/g^{(2)}(T)$) of 0.2 to the broadband emission tail extending from the group of higher-energy PL peaks. The dataset for another chiral QE emitting more than −0.7 DCP and having greater than 95% single-photon purity is shown in Extended Data Fig. 6.

Together, these findings provide clear evidence that the local strain engineering of $WSe_2/NiPS_3$ heterostructures can form QEs capable of generating chiral single photons without the need for an external magnetic field and independent of laser excitation polarization (Figs. 1 and 2 and Extended Data Fig. 3b,c). This observation is fundamentally different from PL polarization ($\rho(B)$) reported to arise from spin-dependent charge transfer in WSe_2/CrI_3 heterostructures[9,10]. These studies compare σ^+-polarized PL detected under near-resonant (1.96 eV) σ^+ laser excitation ($I_{\sigma+/\sigma+}$) with σ^--polarized PL detected under σ^- laser excitation ($I_{\sigma-/\sigma-}$). A non-zero value of $\rho(B) = (I_{\sigma-/\sigma-} - I_{\sigma+/\sigma+})/(I_{\sigma-/\sigma-} + I_{\sigma+/\sigma+})$, therefore, does not indicate the emission of chiral light. In fact, studies of the spin-dependent charge transfer effect in $MoSe_2/CrBr_3$ heterostructures[6,7] that measured DCP independent of excitation laser polarization7 or under linearly polarized laser excitation[7] report no detectable DCP at zero magnetic field. These studies indicate that a simple TMD/MX_3 material system cannot emit chiral classical light. Since these

works[6,7,9,10] primarily focused on the 2D exciton, quantum light (single-photon) emission is not possible. Proximity interaction between the strain-engineered QEs of WSe_2 and 2D magnets such as $Cr_2Ge_3Te_6$ (ref. 5), Fe_3GeTe_2 (ref. 11) and CrI_3 (ref. 8) were recently investigated. No chiral light emission was reported when QEs were coupled to $Cr_2Ge_3Te_6$ (ref. 5) and Fe_3GeTe_2 (ref. 11) (only enhancement in Zeeman splitting[5] and some increase in zero field splitting of the fine-structure states of QEs[11] were reported, respectively). A small value of DCP ≈ 0.15 was observed at zero magnetic field for the localized excitons of WSe_2 coupled to CrI_3 but no photon antibunching was demonstrated[8]. Our demonstration of quantum light emission with DCP up to 0.89 in the absence of an external *B* field and spin-polarized pumping, therefore, clearly stands in contrast with these prior works. Our observations demonstrate the ability of strain-engineered $NiPS_3$ to modify the optical characteristics of QEs via magnetic proximity interactions. Besides immediate relevance for chiral quantum photonics, these results may also be relevant to the long-standing pursuit of spin lasers[15,32] by providing a means to ensure the robust spin polarization of electrons and holes via magnetic proximity effects.

Magnetic proximity interaction evidenced by scanning NV microscopy

Because $NiPS_3$ exhibits zig-zag AFM order with spins aligned parallel or antiparallel to the in-plane *a* axis compensating each other at the lattice constant (Fig. 3a)[22,23,24,26], the net magnetization needed to modify the optical properties of nearby materials through proximity effects is practically averaged out to zero. However, studies have revealed that localized ferromagnetic (FM) moments can emerge in AFM materials due to flexomagnetism (the emergence of net magnetic moments due to bending and/or strain gradients)[33,34] or due to spatial variations in the AFM order parameter, as they occur, for example, in domain walls[35]. Based on these findings, we hypothesize that the magnetic moments of Ni atoms in the strained region around the indentation rotate to point out of plane to form local FM moments due to severe deformations of the $NiPS_3$ lattice and/or changes in the magnetic anisotropy energy. Since the indentation could create localized exciton states in the WSe_2 layer in close vicinity of the local FM moments of $NiPS_3$, the proximity-induced exchange interaction between the FM moments and localized exciton further leads to the time-reversal symmetry breaking necessary for the emission of chiral single photons. Such proximity interaction has been well established on both experimental and theoretical grounds[1,2,36].

To confirm this hypothesis, we imaged the magnetic signal from an indent in a bare $NiPS_3$ flake using a nitrogen-vacancy (NV) centre[37] in a diamond atomic force microscope at $T \approx 4.4$ K (a strong PL background from the WSe_2 monolayer prevented a similar experiment on $WSe_2/NiPS_3$ heterostructures). Topography and magnetic-field images of an indent (Fig. 3c,d) show a magnetic signal of $B_{mean} = 22 \pm 9$ μT from the ridge region surrounding the indentation. The magnetic signal was confirmed by obtaining the full NV lock-in spectra (Methods) both on and off the indent, which indicates a magnetic-field strength of $B_{indent} = 26 \pm 2$ μT (Fig. 3e). A corresponding control experiment that was

conducted at room temperature on the same nanoindentation showed no measurable stray magnetic fields on the sample (Extended Data Fig. 7). This magnetic signal is one order of magnitude weaker compared with that measured on a CrI_3 monolayer[38] and comparable with that arising due to flexomagnetism in AFM Cr_2O_3 films[33]. Because the NV centre is separated from the sample surface by 70 ± 20 nm (standoff distance), the measured field is reduced by inverse vertical-distance scaling and the measurement only yields an average response of the ~70-nm-diameter region directly beneath the NV centre (Fig. 3b). The measured field value, therefore, reflects only a fraction of the actual magnetization on the surface and loss of local fluctuations occurring at length scales of less than 70 nm.

This measurement of the stray magnetic field provides evidence for the emergence of local out-of-plane ferromagnetism in the indented $NiPS_3$ layer below the Néel transition temperature. However, it is crucial to note that the chiral light emission we observed does not arise from the interaction between the stray magnetic field and the QE. Instead, it originates from a proximity-induced magnetic-exchange interaction that occurs when the wavefunction of the localized exciton in WSe_2 overlaps with the electronic wavefunction of Ni ions, forming the local ferromagnetic moment. Since each Ni ion can carry the magnetic moment of the order of $1\mu_B$, the effective magnetic field inducing the chiral emission could be substantially stronger than the measured stray field of local magnetization by a few orders of magnitude. Since the interaction is highly localized and the irregular strain field of nanoindentation could create multiple local magnetizations of varying directionalities and strengths, the QEs from the same indentations display varying directionalities and degrees of circular polarization.

Magnetic proximity interaction evidenced by magneto-PL

To provide further evidence linking our chiral light emission to localized ferromagnetic proximity effects, we performed an additional magneto-optical characterization of the PL emission from nanoindentations in $WSe_2/NiPS_3$ heterostructures. First, we analysed the 1.47 eV ultrasharp exciton emission peak of $NiPS_3$ (refs. 22,23,24), revealing that although the emission is strongly linearly polarized (degree of linear polarization, DLP = 0.76) perpendicular to the Néel vector of $NiPS_3$ on the unstrained region, the DLP of this peak from an indented region drastically reduced to 0.24 and became circularly polarized with DCP = 0.4 (Extended Data Fig. 5). This result indicates the existence of multiple domains with reoriented Néel vectors within an indented region—a prerequisite for the emergence of localized magnetization and ferromagnetic proximity effects.

Studies of $NiPS_3$ have shown that external fields greater than 15 T are required to reorient the Néel vector to the direction of the magnetic field at cryogenic temperatures below the Néel transition temperature ($T_N \approx 150$ K)[23]. Strain-induced localized magnetization associated with AFM defects is, therefore, expected to be stable against external B fields of lesser strength. To test this hypothesis, polarization-resolved PL spectra were acquired from an indentation under external B fields ranging from –6 to +6 T in the Faraday

geometry (Fig. 4a,b and Extended Data Fig. 8). These PL spectra reveal that a strongly circularly polarized PL peak at ~1.59 eV with a DCP of –0.6 exhibits no notable change in DCP as a function of *B* field (Fig. 4b). Consistent with the previous conclusion that the σ^+ and σ^- peaks of the chiral emitter originated from a single electronic state exhibiting incomplete circular polarization, energy splitting between the σ^+ and σ^- peak remains essentially zero for all the *B* fields (Fig. 4b). The spin doublets of localized excitons are known to display *B*-field-dependent, incomplete circular polarization behaviour when strain-induced, anisotropic exchange splitting competes with Zeeman splitting resulting from the external *B* field[30,39] (Supplementary Information). We could interpret the chiral PL peak as the lower-energy state of such a spin doublet. The *B*-field invariance in both PL emission energy and DCP suggests that the magnetic-exchange interaction with FM moments within $NiPS_3$ is dominating over the effect of the external *B* field in inducing valley splitting and chiral quantum light emission. In marked contrast with the localized QE emission, the 2D WSe_2 exciton peak at 1.75 eV displays normal Zeeman splitting (~1.68 meV at ±6 T) similar to uncoupled monolayers, suggesting that proximity interactions average out to zero for delocalized 2D excitons and that chiral PL emission demands the co-localization of exciton and local moments arising from AFM defects.

The defect-induced local magnetic moment in $NiPS_3$ (to which localized excitons in WSe_2 couple), can, however, be influenced by the application of large magnetic fields, if applied at elevated temperatures. These studies are shown in Fig. 4c,d. First, a QE emitting strongly circularly polarized PL at 4 K and $B = 0$ T was identified (1.7 eV PL peak; Fig. 4c). We then raised the temperature to 180 K (above T_N) and applied a +6 T magnetic field along the sample normal. The sample was then cooled back to 4 K and the applied field was maintained at +6 T. The PL spectra acquired after cooling to 4 K at 6 T (Fig. 4c, second row) showed a dramatic decrease in the DCP of QE to ~0.2 from the original value of ~0.7, indicating that the local magnetization responsible for the QE's chiral PL emission is reduced, probably as a consequence of the applied *B* field opposing the local moment's preferred orientation direction. When the external *B* field is decreased, the DCP was found to increase until it was fully restored to its original value at 0 T (Fig. 4c,e and Extended Data Fig. 9), suggesting that the local strain distribution and underlying AFM order restores the original local magnetization in the absence of an external field. In contrast, when a *B* field in the opposite direction (–6 T) is applied at 180 K, no notable change in the DCP of QE is observed since *B* aligns parallel to the preferred local magnetization, making it more stable (Fig. 4d,e). Importantly, in both cases, the chiral emission is restored at $B = 0$ T, and sweeping the fields from +6 to –6 T after the restoration of chiral emission at 0 T (Extended Data Fig. 9e,f) reproduces the *B*-field-independent behaviour of chiral QE (Fig. 4a). This restoration of chiral emission and thermal hysteresis behaviour indicate that the underlying AFM order is unaffected by ±6 T applied fields, as expected. This experiment provides strong evidence that our chiral QEs form due to proximity interactions with localized out-of-plane magnetizations that are intimately tied to FM moments in $NiPS_3$ and

AFM order of the surrounding $NiPS_3$ stabilized the orientation and strength of the FM moments against the external *B* field.

In summary, our observations reveal that local strain engineering can be utilized not only to create QEs but also to localize ferromagnetic proximity effects required for the creation of chiral single-photon emitters in $WSe_2/NiPS_3$ heterostructures. Interestingly, a similar chiral localized excitonic emission was also observed in our more recent experiment performed on $WSe_2/MnPS_3$ and $WSe_2/FePS_3$ heterostructures with nanoindentations (Extended Data Fig. 10). These discoveries establish $TMD/TMPX_3$ AFM insulators as an exciting material platform for the further exploration of novel emergent phenomena and the realization of solid-state quantum transduction and sensing technologies.

Methods

Sample preparation

A PMMA solution was spin coated on a Si substrate with a 285 nm SiO_2 layer to achieve a 300-nm-thick uniform membrane. $NiPS_3$ flakes were exfoliated from bulk crystals (2D Semiconductors) using Scotch tape and deposited onto the PMMA layer. Monolayers of WSe_2 (HQ Graphene) were mechanically exfoliated onto a silicone Gel-Film stamp. The layer thickness was identified by optical microscopy contrast and room-temperature PL. The WSe_2 monolayers were then transferred onto the selected $NiPS_3$ flakes using a 2D material transfer system from HQ Graphene. $NiPS_3$ and WSe_2 exfoliations as well as layer stacking were performed in an argon-filled glove box to minimize degradation. Once the heterostructure was fabricated, nanoindentations were deterministically created by using a Bruker Dimension Icon instrument using blunt atomic force microscopy probes with a nominal tip radius of 100 nm and a spring constant of 80 N m^{-1}. Indentations were fabricated by performing approach curves with a maximum force setpoint between 50 and 60 μN. This combination of probe radius and force setpoint was found to consistently produce chiral QEs within the $WSe_2/NiPS_3$ heterostructures. Topography imaging of the surface following nanoindentation was performed using tapping-mode imaging with a second, higher-resolution topography probe (tip radius, ~10 nm).

Low-temperature polarization-resolved PL spectroscopy and Hanbury Brown–Twiss experiments

The schematic of the experimental setup for optical measurements is illustrated in Extended Data Fig. 1. The sample was held at 4 K in a continuous-flow cryostat (Oxford Instruments, MicrostatHires). The heterostructures were excited with a 514 nm continuous-wave laser (Coherent OBIS) and the PL signal was collected through a ×50, 0.55-numerical-aperture Olympus microscope objective. A quarter-wave plate (QWP) was placed immediately after the objective to circularly polarize the laser excitation and converted the σ^+- and σ^--polarized PL signal into *S* and *P* linear polarization. A Wollaston prism was then used to split the signal into channels, which were then projected onto a

liquid-nitrogen-cooled charge-coupled device detector through a 500 mm spectrometer (Acton SpectraPro). This arrangement allowed the simultaneous collection of the spectral images of σ^+ and σ^- PL signals on two different portions of the charge-coupled device camera (Extended Data Fig. 1). The σ^+ and σ^- PL spectra and the extracted DCP are, therefore, free of artifacts that could result from random intensity fluctuations and spectral wandering. For linear polarization analysis, the QWP was removed, and two half-wave plates (HWP1 and HWP2) were inserted in the excitation and collection channels before the Wollaston prism. The PL spectra were acquired as a function of the rotation angles of the half-wave plates to determine the degree and orientation of PL linear polarization. HWP2 was replaced with a QWP to acquire σ^+- and σ^--polarized PL spectra under linearly polarized excitation (Extended Data Fig. 3). For the time-tagged time-correlated PL measurements, we pumped the sample with a tunable visible picosecond laser (TOPTICA Photonics, 40 MHz repetition rate, 3.5 ps pulse width) filtered by a 10 nm band-pass filter centred at 514 nm. The emission was then filtered by using a tunable band-pass filter (SLI) and coupled into a Hanbury Brown–Twiss spectrometer composed of a 50/50 beamsplitter and two avalanche photodiodes (MPD PDM Series) with a timing accuracy of 35 ps. The macro- and microtimes of each photon detection event were recorded with a HydraHarp 400 time-correlated single-photon counting module and the PL intensity time traces, PL lifetime and second-order photon correlation ($g^{(2)}(\tau)$) were extracted from the recorded photon stream. Here $g^{(2)}(\tau)$ depicts the probability of registering two successive photons as a function of the time delay (τ) between the detection events. Under pulsed laser excitation, the $g^{(2)}$ trace displays a periodic series of peaks separated by the delay time between the laser excitation pulses. These peaks indicate the detection of two successive photons that result from excitation by different laser pulses. Since a single QE can only produce at most one photon per pulsed excitation, the peak at zero delay time ($g^{(2)}(0)$) should be completely absent. The $g^{(2)}$ trace in Fig. 2e shows the $g^{(2)}(0)$ peak with an area of 20% compared with the side peak. This fact indicates that our chiral QE produces single photons 80% of the time.

Scanning diamond NV-centre magnetometry imaging

To perform local magnetometry on the $NiPS_3$, a new $WSe_2/NiPS_3$ heterostructure on PMMA was prepared with nanoindents on both pure $NiPS_3$ and $WSe_2/NiPS_3$ heterostructures. The sample was mounted inside a combined optical and atomic force microscope housed in a cryostat (attoLIQUID1000) where the atomic force microscope sensor consisted of a diamond and hosted the sensing NV at its tip (Qnami, Quantilever MX)[38]. All the measurements were performed at an approximate temperature of $T \approx 4.4$ K. The NV centre was excited with a 532 nm laser to optically polarize the NV spin and to read out the spin state via a spin-state-dependent PL, whereas the electron spin was driven with a frequency-tunable microwave source to record the electron spin resonance spectra. To reduce the background light from the sample, a 600 nm long-pass filter and a 700 nm short-pass filter (Thorlabs) were used before the avalanche photodiode detector. At each position, a lock-in measurement is performed to attain the Larmor precession frequency of the electron spin,

which is determined by the magnetic-field projection along the NV axis (inclined at 60° with respect to the sample normal) through the Zeeman splitting of the NV spin's energy levels40. The lock-in measurement works by introducing a frequency modulation to the microwave driving field that rapidly samples two frequencies that are offset by the measured linewidth of the NV spectrum. The difference in these two frequencies forms the feedback signal that linearly depends on the stray magnetic field, within a certain dynamic range (Fig. 3e). The NV-containing diamond probe has an ~500 nm tip diameter[41] and the NV centre is separated from the sample surface by a 70 ± 20 nm standoff distance. Although the height image can, therefore, not fully resolve the indentation, the key features in the ridge area can be identified via a direct comparison with the high-resolution AFM image taken on a different system. The standoff distance leads to an inverse-distance-scale-down measured *B* field[42] and limits the lateral resolution to 70 ± 20 nm with an additional blurring of the edge features by 250 nm assuming that the NV centre is located close to the centre of the 500-nm-diameter tip. The measurement of the *B* field surrounding the indents of the $WSe_2/NiPS_3$ heterostructures was not feasible due to the strong optical background associated with the PL emission from the WSe_2 monolayer.

Temperature-dependent magneto-PL experiment

To perform the magneto-PL experiments, the sample was mounted in the variable-temperature insert of a 7 T magneto-optical cryostat (Oxford Instruments Spectramag). An in situ aspheric lens (numerical aperture = 0.68), mounted on piezoelectric nanopositioners (attocube), focused the incident light. The sample was excited using a continuous-wave 632.8 nm HeNe laser. The polarization of the laser was controlled using a QWP and a linear polarizer. Emission from the sample in the Faraday geometry was collected by the same aspheric lens, and its polarization was analysed using a QWP and linear polarizers. The emission was dispersed in a 500 mm spectrometer (Acton) and detected by a liquid-nitrogen-cooled charge-coupled device detector. For the temperature-dependent magneto-PL measurements, we first set the sample temperature to 180 K (above the Néel temperature of the $NiPS_3$) and then ramped the magnetic field to either +6 or –6 T. The sample was then cooled back to 4 K to repeat the field-ramping experiments.

Acknowledgements

This work was performed at the Center for Integrated Nanotechnologies, an Office of Science User Facility, operated for the US Department of Energy (DOE) Office of Science (OS). Los Alamos National Laboratory (LANL), an affirmative action equal opportunity employer, is managed by Triad National Security LLC for the US DOE's NNSA, under contract 89233218CNA000001. Laboratory Directed Research and Development (LDRD) program 20200104DR provided primary support for the works of X.L., H.Z., A.P., N.S., S.A.C. and H.H. A.C.J. and V.C. acknowledge support from the DOE Basic Energy Sciences, QIS Infrastructure Development Program, Deterministic Placement and Integration of Quantum Defects. X.L., H.H. and S.A.C. also acknowledge partial support by the Quantum Science Center, a National QIS Research Center supported by the DOE, OS. J.C. and H.Z. also

acknowledge partial support from LANL Director's Postdoctoral Fellow Award. M.T.P. acknowledges support from LDRD awards 20210782ER and 20210640ECR. The National High Magnetic Field Laboratory is supported by the National Science Foundation (NSF) DMR-1644779, the State of Florida, and the US DOE. P.M., D.A.B., M.A.T. and P.R. acknowledge financial support from the National Centre of Competence in Research (NCCR) Quantum Science and Technology (QSIT), a competence centre funded by the Swiss National Science Foundation (SNF), by SNF project no. 188521, and by the ERC consolidator grant project QS2DM. We would like to acknowledge B. Zhou and X. Zhang for the magnetometry experiments using a near-surface ensemble of NV centres, and E. Peterson and C. A. Lane for insightful discussions on the magnetic-exchange proximity interaction.

Contributions

H.H. conceived and led the experiment. X.L., under the supervision of H.H., initiated the idea of using the nanoindentation method for enhancing the magnetic proximity effect along with the deterministic creation of localized QEs, prepared the samples and conducted the experiments. A.C.J. guided X.L. in creating nanoindentations in the $WSe_2/NiPS_3$ heterostructure and scanning probe microscopy studies. S.A.C. contributed the key idea of the temperature-dependent magneto-PL experiment and X.L. and J.C. conducted the experiment. H.Z., M.T.P. and V.C. assisted X.L. in a variety of optical spectroscopy experiments. N.S. and A.P. provided the theoretical model. D.A.B., M.A.T. and P.R. performed the NV magnetometry measurements under the supervision of P.M. H.H. and X.L. wrote the manuscript with the assistance of all the authors.

References

1 Žutić, I., Matos-Abiague, A., Scharf, B., Dery, H. & Belashchenko, K. Proximitized materials. Mater. Today 22, 85–107 (2019).

2 Huang, Y. et al. Room-temperature electron spin polarization exceeding 90% in an opto-spintronic semiconductor nanostructure via remote spin filtering. Nat. Photon. 15, 475–482 (2021).

3 Scharf, B., Xu, G., Matos-Abiague, A. & Žutić, I. Magnetic proximity effects in transition-metal dichalcogenides: converting excitons. Phys. Rev. Lett. 119, 127403 (2017).

4 Zhao, C. et al. Enhanced valley splitting in monolayer WSe2 due to magnetic exchange field. Nat. Nanotechnol. 12, 757–762 (2017).

5 Shayan, K. et al. Magnetic proximity coupling of quantum emitters in WSe2 to van der Waals ferromagnets. Nano Lett. 19, 7301–7308 (2019).

6 Ciorciaro, L., Kroner, M., Watanabe, K., Taniguchi, T. & Imamoglu, A. Observation of magnetic proximity effect using resonant optical spectroscopy of an electrically tunable MoSe2/CrBr3 heterostructure. Phys. Rev. Lett. 124, 197401 (2020).

7 Lyons, T. P. et al. Interplay between spin proximity effect and charge-dependent exciton dynamics in MoSe2/CrBr3 van der Waals heterostructures. Nat. Commun. 11, 6021 (2020).

8 Mukherjee, A. et al. Observation of site-controlled localized charged excitons in CrI3/WSe2 heterostructures. Nat. Commun. 11, 5502 (2020).

9 Zhong, D. et al. Layer-resolved magnetic proximity effect in van der Waals heterostructures. Nat. Nanotechnol. 15, 187–191 (2020).

10 Zhong, D. et al. Van der Waals engineering of ferromagnetic semiconductor heterostructures for spin and valleytronics. Sci. Adv. 3, e1603113 (2017).

11 Liu, N. et al. Antiferromagnetic proximity coupling between semiconductor quantum emitters in WSe2 and van der Waals ferromagnets. Nanoscale 13, 832–841 (2021).

12 Tu, Z. et al. Spin–orbit coupling proximity effect in MoS2/Fe3GeTe2 heterostructures. Appl. Phys. Lett. 120, 043102 (2022).

13 Mak, K. F., Xiao, D. & Shan, J. Light–valley interactions in 2D semiconductors. Nat. Photon. 12, 451–460 (2018).

14 Aivazian, G. et al. Magnetic control of valley pseudospin in monolayer WSe2. Nat. Phys. 11, 148–152 (2015).

15 Lindemann, M. et al. Ultrafast spin-lasers. Nature 568, 212–215 (2019).

16 Seyler, K. L. et al. Signatures of moiré-trapped valley excitons in MoSe2/WSe2 heterobilayers. Nature 567, 66–70 (2019).

17 Tran, K. et al. Evidence for moiré excitons in van der Waals heterostructures. Nature 567, 71–75 (2019).

18 Chen, D., He, R., Cai, H., Liu, X. & Gao, W. Chiral single-photon generators. ACS Nano 15, 1912–1916 (2021).

19 Lodahl, P. et al. Chiral quantum optics. Nature 541, 473–480 (2017).

20 Li, H., Ruan, S. & Zeng, Y.-J. Intrinsic van der Waals magnetic materials from bulk to the 2D limit: new frontiers of spintronics. Adv. Mater. 31, 1900065 (2019).

21 Kim, S. Y. et al. Charge-spin correlation in van der Waals antiferromagnet NiPS3. Phys. Rev. Lett. 120, 136402 (2018).

22 Kang, S. et al. Coherent many-body exciton in van der Waals antiferromagnet NiPS3. Nature 583, 785–789 (2020).

23 Wang, X. et al. Spin-induced linear polarization of photoluminescence in antiferromagnetic van der Waals crystals. Nat. Mater. 20, 964–970 (2021).

24 Hwangbo, K. et al. Highly anisotropic excitons and multiple phonon bound states in a van der Waals antiferromagnetic insulator. Nat. Nanotechnol. 16, 655–660 (2021).

25 Ni, Z. et al. Imaging the Néel vector switching in the monolayer antiferromagnet MnPSe3 with strain-controlled Ising order. Nat. Nanotechnol. 16, 782–787 (2021).

26 Kim, K. et al. Suppression of magnetic ordering in XXZ-type antiferromagnetic monolayer NiPS3. Nat. Commun. 10, 345 (2019).

27 Clerk, A. A., Lehnert, K. W., Bertet, P., Petta, J. R. & Nakamura, Y. Hybrid quantum systems with circuit quantum electrodynamics. Nat. Phys. 16, 257–267 (2020).

28 Onga, M. et al. Antiferromagnet–semiconductor van der Waals heterostructures: interlayer interplay of exciton with magnetic ordering. Nano Lett. 20, 4625–4630 (2020).

29 Rosenberger, M. R. et al. Quantum calligraphy: writing single-photon emitters in a two-dimensional materials platform. ACS Nano 13, 904–912 (2019).

30 Turunen, M. et al. Quantum photonics with layered 2D materials. Nat. Rev. Phys. 4, 219–236 (2022).

31 Peyskens, F., Chakraborty, C., Muneeb, M., Van Thourhout, D. & Englund, D. Integration of single photon emitters in 2D layered materials with a silicon nitride photonic chip. Nat. Commun. 10, 4435 (2019).

32 Žutić, I. et al. Spin-lasers: spintronics beyond magnetoresistance. Solid State Commun. 316–317, 113949 (2020).

33 Makushko, P. et al. Flexomagnetism and vertically graded Néel temperature of antiferromagnetic Cr2O3 thin films. Nat. Commun. 13, 6745 (2022).

34 Andreev, A. F. Macroscopic magnetic fields of antiferromagnets. J. Exp. Theor. Phys. 63, 758–762 (1996).

35 Hedrich, N. et al. Nanoscale mechanics of antiferromagnetic domain walls. Nat. Phys. 17, 574–577 (2021).

36 Peterson, E. A., Haber, J. B. & Neaton, J. B. Superexchange-induced valley splitting in two-dimensional transition metal dichalcogenides: a first-principles study for rational design. Phys. Rev. B 104, 205421 (2021).

37 Doherty, M. W. et al. The nitrogen-vacancy colour centre in diamond. Phys. Rep. 528, 1–45 (2013).

38 Thiel, L. et al. Probing magnetism in 2D materials at the nanoscale with single-spin microscopy. Science 364, 973–976 (2019).

39 Htoon, H. et al. Anomalous circular polarization of photoluminescence spectra of individual CdSe nanocrystals in an applied magnetic field. Phys. Rev. Lett. 102, 017402 (2009).

40 Balasubramanian, G. et al. Nanoscale imaging magnetometry with diamond spins under ambient conditions. Nature 455, 648–651 (2008).

41 Hedrich, N., Rohner, D., Batzer, M., Maletinsky, P. & Shields, B. J. Parabolic diamond scanning probes for single-spin magnetic field imaging. Phys. Rev. Appl. 14, 064007 (2020).

42 Tetienne, J.-P. et al. The nature of domain walls in ultrathin ferromagnets revealed by scanning nanomagnetometry. Nat. Commun. 6, 6733 (2015).

Figures

Fig. 1: Strain-engineered $WSe_2/NiPS_3$ heterostructures host QEs displaying sharp, localized PL peaks with a strong degree of spontaneous circular polarization

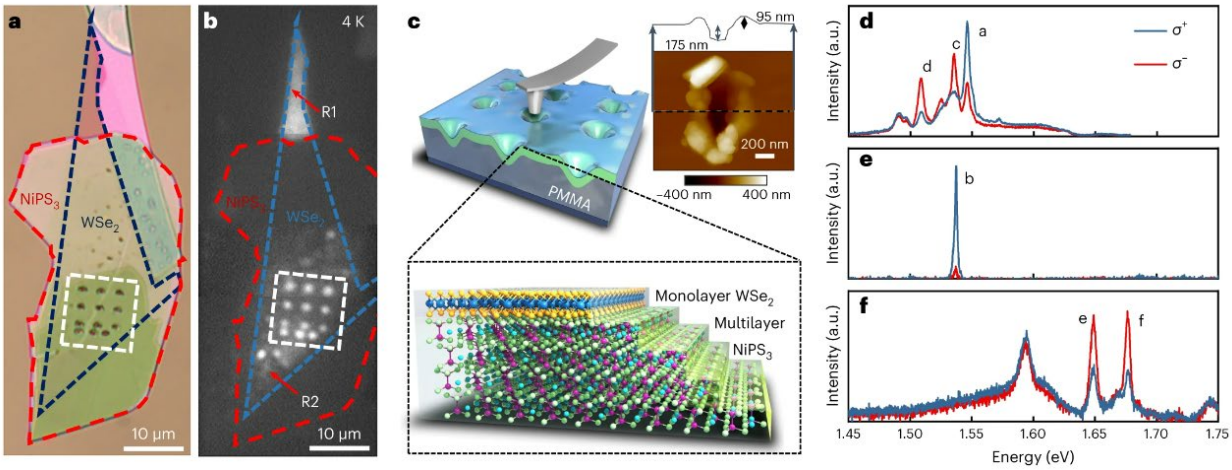

a,**b**, Optical (**a**) and PL (**b**) images of a $WSe_2/NiPS_3$ heterostructure. The portion of the WSe_2 monolayer that does not overlap with $NiPS_3$ emits bright PL (region R1), whereas PL is quenched when the WSe_2 is coupled to the $NiPS_3$ (region R2). Strong PL was restored by indentations marked by the white square. **c**, Schematic of the sample structure and an atomic force microscopy topography image and cross section of a representative indentation (inset). **d**–**f**, Representative σ^+-resolved (blue) and σ^--resolved (red) PL spectra from different individual nanoindentations acquired under linearly polarized laser excitation at 4 K. Although the peaks marked as a and b are σ^+ polarized with DCP values of 0.36 and 0.89, peaks marked c–f are σ^- polarized with DCP values of –0.40, –0.29, –0.33 and –0.37, respectively. Some of the localized emission peaks ride on top of a broad PL background that displays little polarization, suggesting that the DCP of localized emission peaks could even be higher if the broad PL background is subtracted.

Fig. 2: Demonstration of quantum light emission from strain-engineered $WSe_2/NiPS_3$ heterostructures

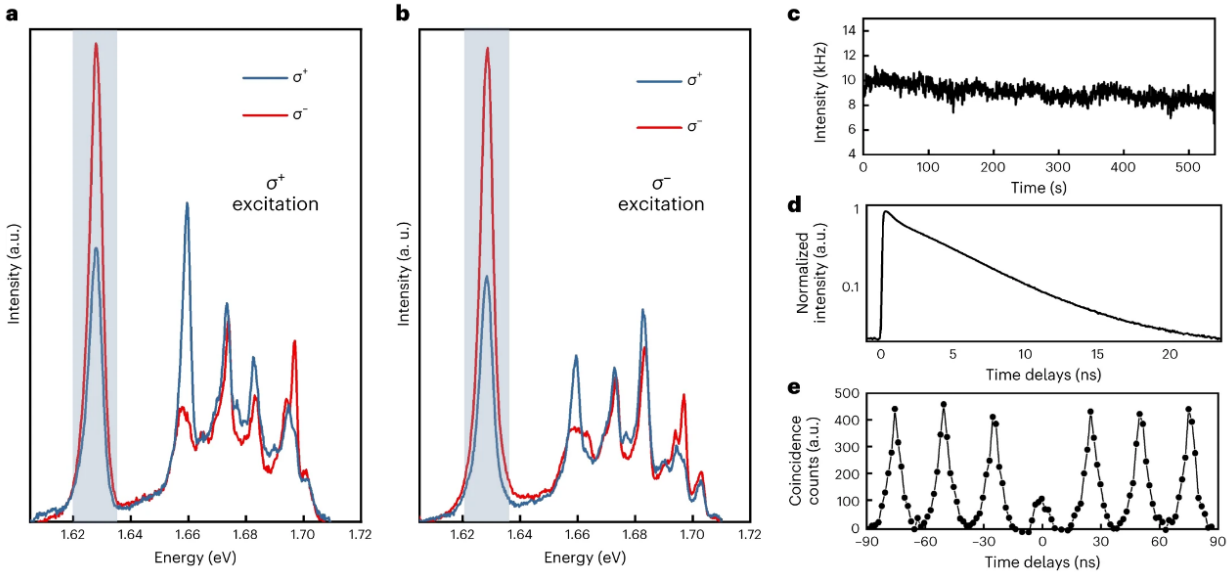

a,**b**, σ^+-polarized (blue) and σ^--polarized (red) PL spectra of an indented $WSe_2/NiPS_3$ heterostructure acquired under σ^+-polarized (**a**) and σ^--polarized (**b**) laser excitation. **c**–**e**, PL intensity time trace (**c**), PL decay curve (**d**) and second-order photon correlation trace (**e**) measured from the PL peak marked by the blue column in **a** and **b** acquired under 514 nm, 40 MHz pulsed laser excitation.

Fig. 3: Correlation of chiral quantum light emission with local magnetization

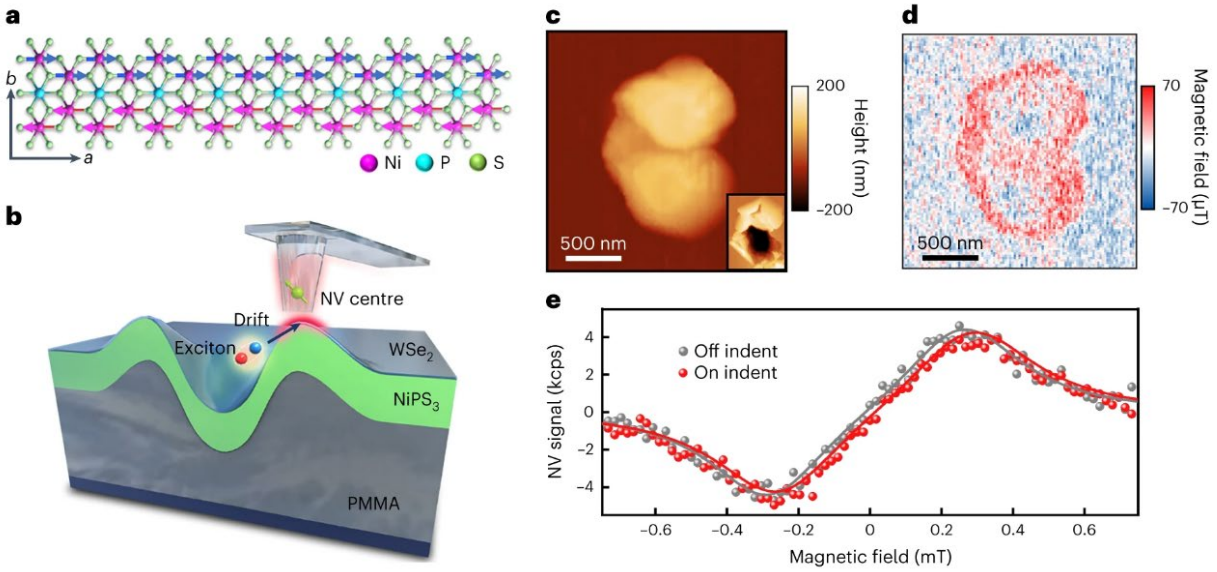

a, Zig-zag AFM order overlaid with the atomic $NiPS_3$ structure where Ni electronic spins are aligned parallel (blue arrows) and antiparallel (red arrows) to the crystallographic *a* axis. **b**, Schematic of an indentation region cross section where the local strain creates exciton-capture centres in WSe_2. **c**,**d**, Scanning NV-centre mapping of the surface magnetization

associated with the morphology of a nanoindentation (**c**) is strongly correlated with the magnetic field measured in the indentation region (**d**). **e**, NV spectra taken both off (grey) and on (red) the indented region show a shift in the detected magnetic signal of B_{indent} = 26 ± 2 μT. A high-resolution atomic force microscopy image of the nanoindentation is provided (inset of **c**) as the NV scanning probes have reduced spatial resolution. The scanning NV centre has a standoff distance of 70 ± 20 nm, meaning that the measured magnetic field is reduced by spatial averaging and inverse distance scaling. kcps, kilo counts per second.

Fig. 4: Magneto-PL studies of chiral QEs

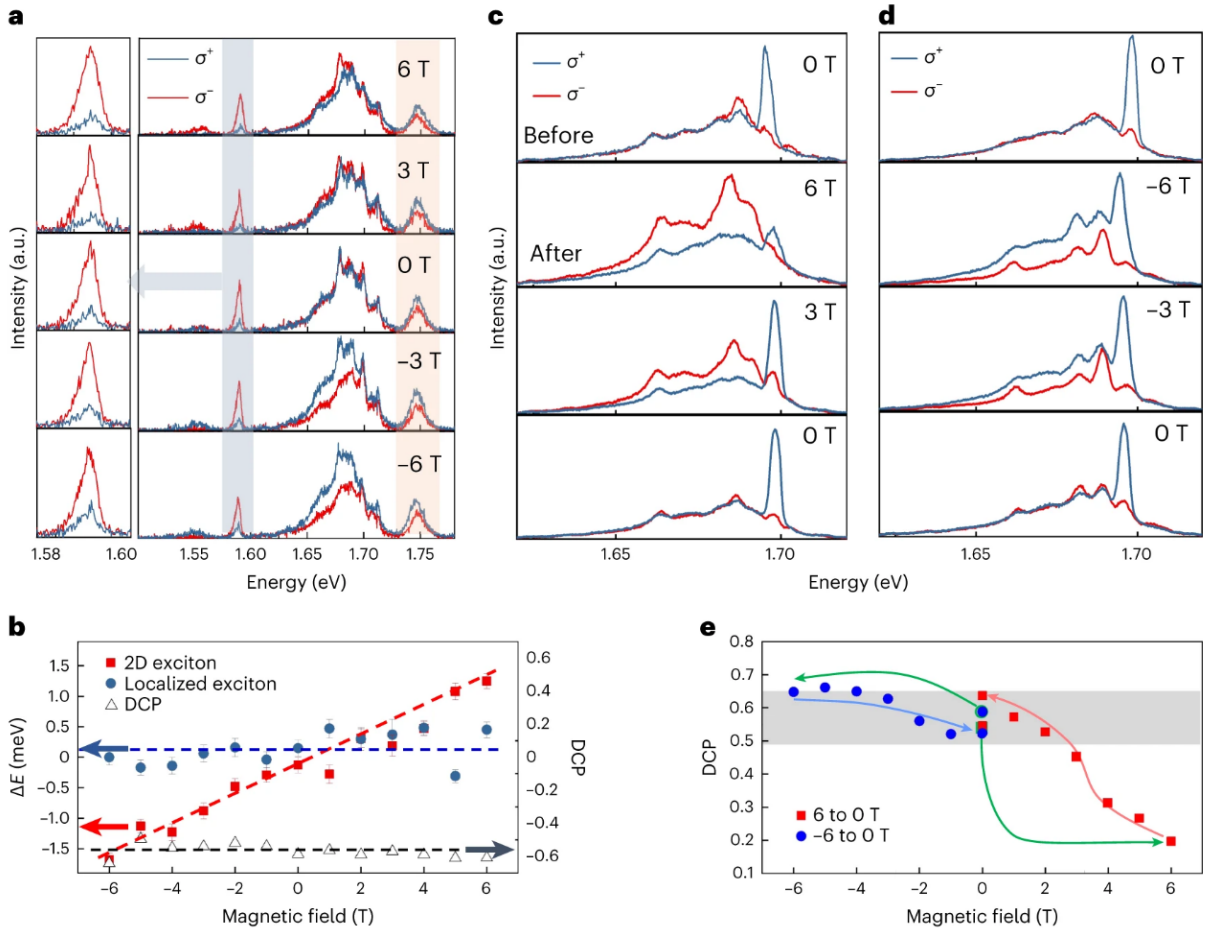

a, Low-temperature, polarization-resolved PL spectra acquired as a function of external *B* field applied perpendicular to the sample plane (Faraday geometry). An expanded view of a localized PL peak (1.59 eV; grey bar) displays a strong DCP of –0.6 (left). **b**, Energy splitting (left axis) between the σ^+ and σ^- PL peaks of a localized exciton at 1.59 eV (blue data points) and a 2D exciton at 1.75 eV (red data points). The error bars represent the uncertainty in the peak positions determined by the Gaussian fit. The DCP (right axis) of the 1.59 eV peak versus *B* field is plotted as black triangles. The blue, red and black dashed lines are guides to the eye. **c**, Low-temperature, polarization-resolved PL

spectra of an indented region with a PL peak at ~1.70 eV, exhibiting a strong DCP of ~0.7 before the temperature- and field-dependent measurement (top row). Low-temperature, polarization-resolved PL spectra of the same location acquired after heating the sample to 180 K, raising the field to 6 T and cooling the sample back down to 4 K while maintaining *B* at 6 T (second row). Low-temperature, polarization-resolved PL spectra acquired as the field is reduced back to 0 T (two bottom rows). **d**, The experiment in **c** was repeated by applying an external field of –6 T at 180 K. **e**, DCP of the 1.69 eV peak plotted against an external *B* field. The green arrows originate from the DCP value originally observed in the top-most panels of **c** and **d** and indicate the process involving heating the sample to 180 K and cooling back down to 4 K while maintaining the *B* field at 6 T (–6 T). The red (blue) arrows and data points represent the process and DCP observed during the reduction in *B* from 6 T (–6 T) to 0 T at 4 K immediately after cooling down. Since the DCP values are calculated from the peak intensities of the $\sigma^{+/-}$-polarized spectra, they are contributed not only by the QE emission but also by the broad PL background that increases as the field is ramped from +6 to –6 T. The grey-shaded region represents variations in the DCP measured at 0 T.

Extended Data Figures

Extended Data Fig. 1: Experimental setup for low-temperature polarization resolved PL spectroscopy

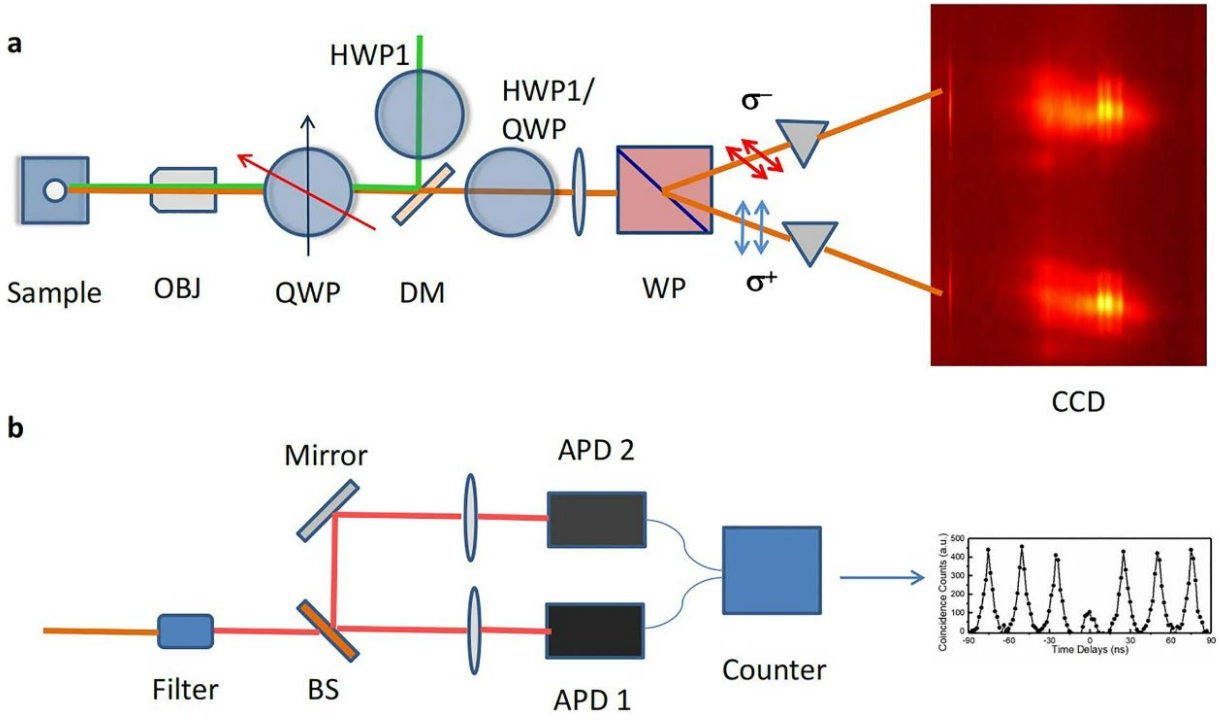

a. OBJ: Objective, DM: Dichroic mirror, QWP: quarter-wave plate, WP: Wollaston prism. For the linear polarization measurements, QWP is removed and two half-wave plates (HWP1 and HWP2) are inserted in excitation and collection channels. **b**. Schematic of the HBT

experiment. BS: 50/50 beam splitter, APD1, APD2: Avalanche photo diodes, Counter: Hydra400 TCSPC module.

Extended Data Fig. 2: Control experiments

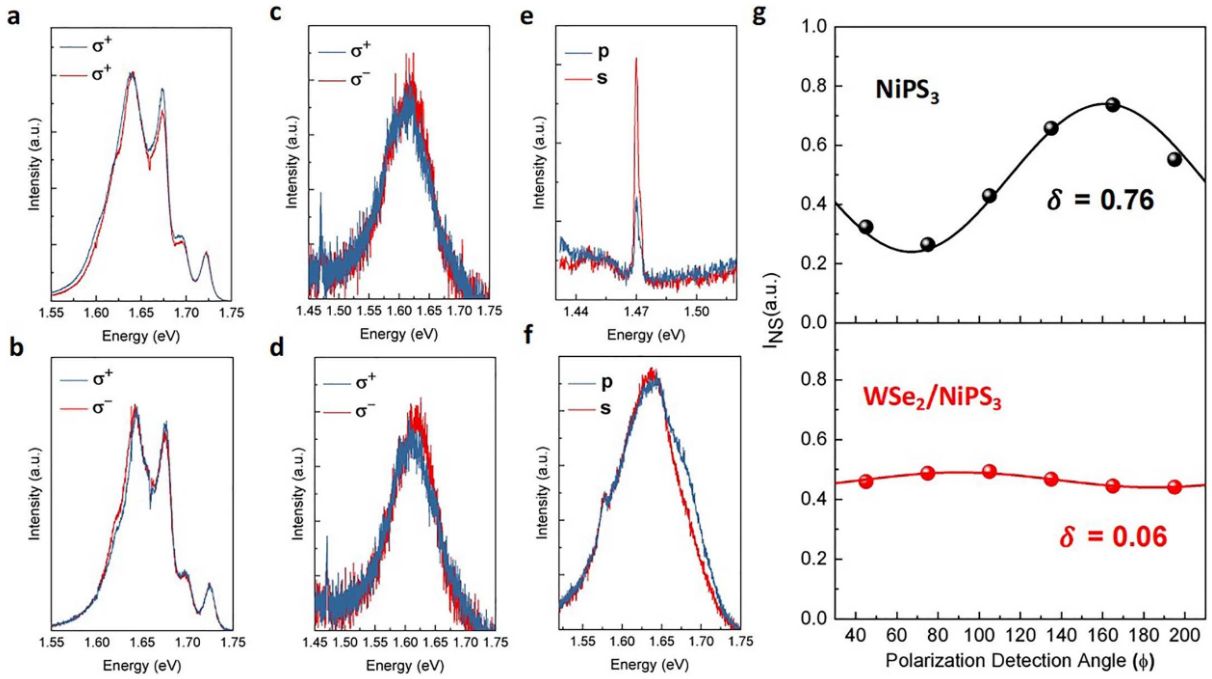

a-d. Low temperature, $\sigma^{+/-}$ polarized PL spectra of WSe_2 monolayer, region R1 of Fig. 1b**(a, b)** and un-indented $WSe_2/NiPS_3$ heterostructure, region R2 of Fig. 1b**(c, d)** excited by σ^+ **(a, c)** and σ^- **(b, d)** 514 nm laser. The data show no detectable DCP in the emission of both monolayer and un-indented $WSe_2/NiPS_3$ hetrostructure indicating that spin-polarized excitons injected at 514 nm were depolarized completely upon relaxation to the band-edge. **e, f**. Low temperature, linearly (S, P) polarized PL spectra (left panel) and plot of DLP as the function of polarization detection angle (right panel) for the sharp emission peak at 1.47 eV **(e)** and WSe_2 exciton emission **(f)**. **(g) Upper Panel**. Strong DLP (0.76) observed for 1.47 eV sharp emission peak is consistent with prior studies that attributed the emission to highly anisotropic excitons reflecting the emergence of AFM order in $NiPS_3$. **Lower Panel**. PL of unstrained $WSe_2/NiPS_3$ heterostructure shows a weak degree of linear polarization consistent with the behavior of WSe_2 monolayer.

Extended Data Fig. 3: Control experiment and invariance of circularly polarized PL emission under laser excitation of different polarization

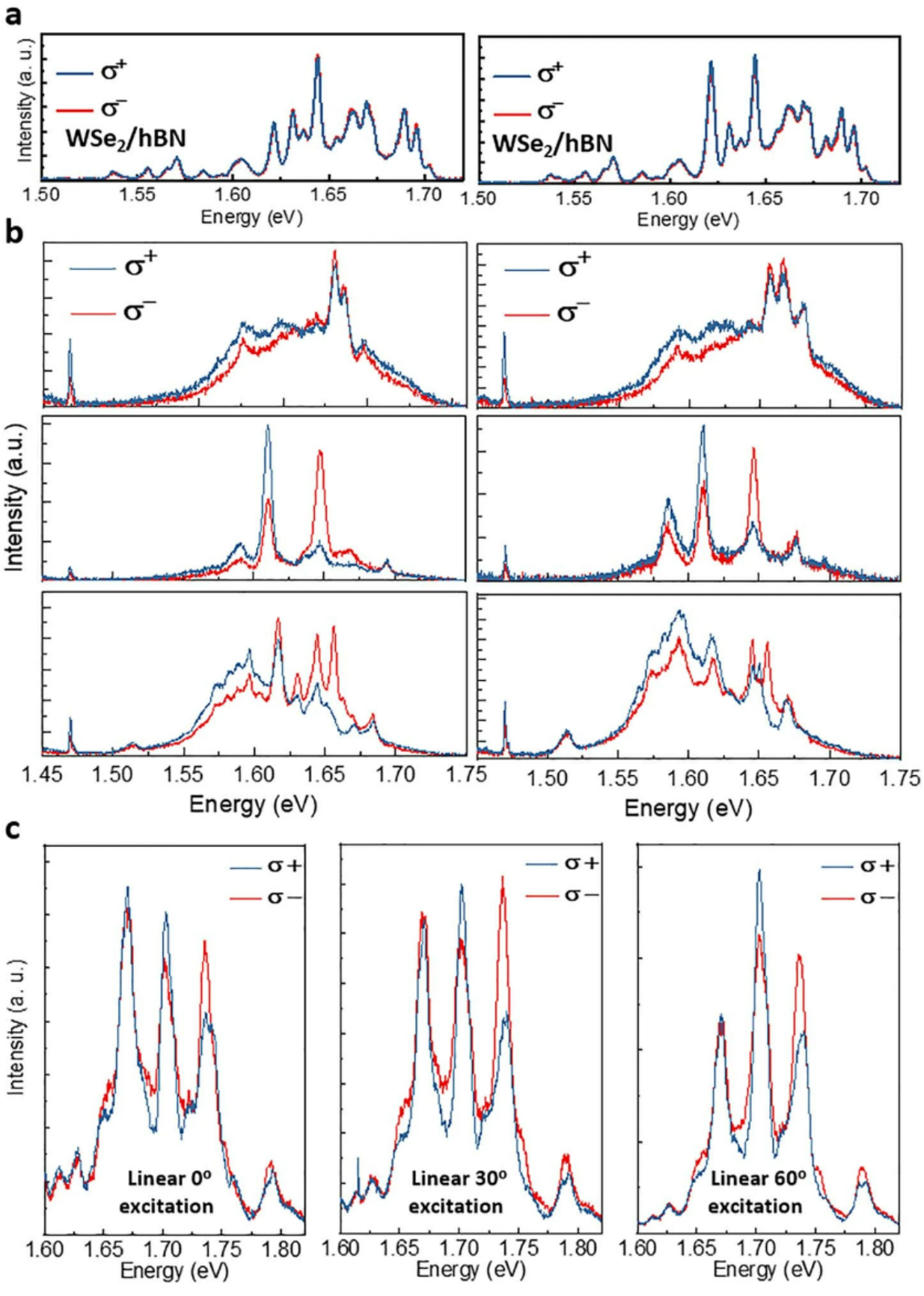
a
Intensity (a. u.)
σ+
σ−
WSe2/hBN
1.50 1.55 1.60 1.65 1.70
Energy (eV)
σ+
σ−
WSe2/hBN
1.50 1.55 1.60 1.65 1.70
Energy (eV)
b
σ+
σ−
σ+
σ−
Intensity (a.u.)
1.45 1.50 1.55 1.60 1.65 1.70 1.75
Energy (eV)
1.50 1.55 1.60 1.65 1.70 1.75
Energy (eV)
c
Intensity (a. u.)
σ+
σ−
Linear 0° excitation
1.60 1.65 1.70 1.75 1.80
Energy (eV)
σ+
σ−
Linear 30° excitation
1.60 1.65 1.70 1.75 1.80
Energy (eV)
σ+
σ−
Linear 60° excitation
1.60 1.65 1.70 1.75 1.80
Energy (eV)

a. σ^+/σ^- polarization resolved PL spectra from WSe_2/hBN/PMMA structures with similar nano-indents of Fig. 1, acquired under σ^+(left) and σ^- (right) polarized laser excitation, respectively. While localized exciton emission peaks of similar line shapes were created, no circularly polarized emission were detected. **b**. σ^+/σ^- polarization resolved PL spectra from 3 nano-indents of Fig. 1a, b acquired under σ^+(left) and σ^- (right) polarized laser excitation, respectively. While most nano-indents show circularly polarized localized exciton emission (bottom two panels), some show no circular polarization (top panels). When the excitation laser polarization is switched from σ^+ to σ^-, the polarities of the circularly polarized emission peak remain the same (peak marked *a* and *b*) but some quantitative change in DCPs as well as relative intensities of the localized PL peaks occur. **c**. Circularly polarized PL emission also remain qualitatively the same when the orientation of linearly polarized PL excitation is changed from 0 – 60 degree.

Extended Data Fig. 4: Spectral image and analysis of the spatial distribution of PL intensity

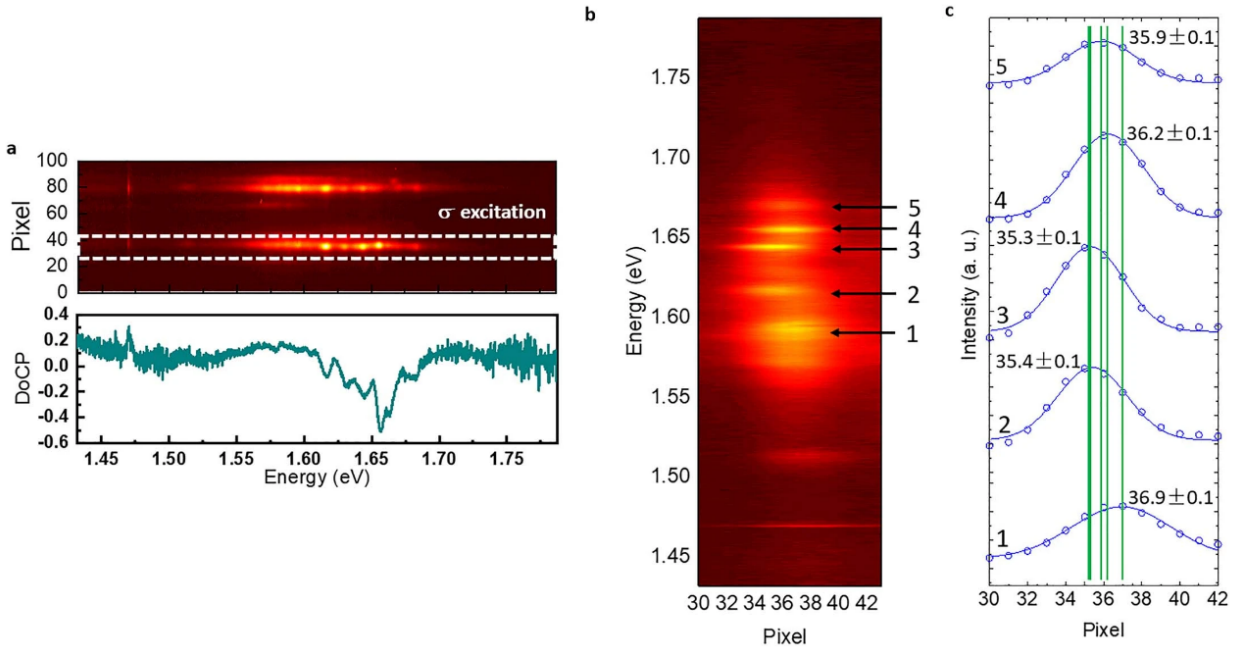

a. PL spectral image of a nanoindentation in Fig. 1 a,b. σ^+ and σ^- PL emissions are simultaneously recorded on two different regions of the CCD array **(upper)**. Degree of circular polarization (DoCP) spectrum calculated from integrated σ^+ and σ^- PL spectra **(lower)**. **b**. Magnified spectra image of the region marked in (a)**. c**. Blue data points: Intensity distribution of the localized emission peaks marked 1-5 in (b). By fitting the PL intensity distribution with Gaussian function (black fitted curves), we can determine the centroid of the emission peak with ± 0.1 pixel precision. The position of each peak and fitting error is listed next to the peak. Based on the magnification factor of the microscope objective (50X) and pixel dimensions of the CCD (20 μm), we can estimate that all peaks,

marked 1- 5 originated from slightly different locations around the nano-indents. The separation between Peak 2 and 3 is ~ 50 nm.

Extended Data Fig. 5: Analyzing linear polarization of strain-engineered WSe2/NiPS3 heterostructure and distribution of linewidth of chiral quantum emitters and pump-dependent measurements

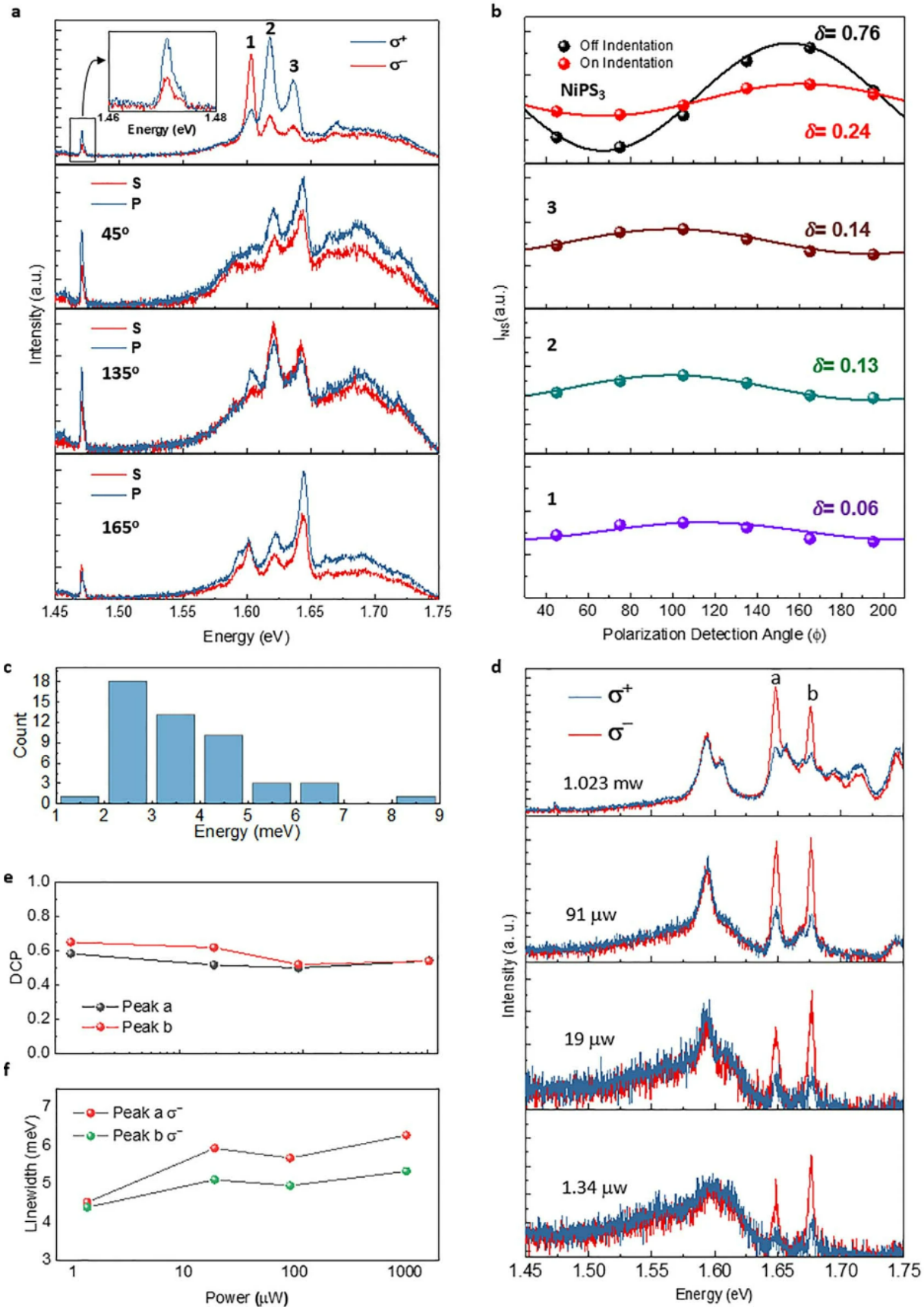
a
1
2
3
σ+
σ−
1.46
1.48
Energy (eV)
S
P
45°
135°
165°
Intensity (a.u.)
1.45
1.50
1.55
1.60
1.65
1.70
1.75
Energy (eV)
b
Off Indentation
On Indentation
NiPS3
δ= 0.76
δ= 0.24
3
δ= 0.14
2
δ= 0.13
1
δ= 0.06
INS(a.u.)
40
60
80
100
120
140
160
180
200
Polarization Detection Angle (ϕ)
c
Count
Energy (meV)
d
σ+
σ−
a
b
1.023 mw
91 μw
19 μw
1.34 μw
Intensity (a. u.)
Energy (eV)
e
DCP
Peak a
Peak b
f
Linewidth (meV)
Peak a σ−
Peak b σ−
Power (μW)

a, top panel. σ^+/σ^- polarized PL spectra acquired under σ^+ excitation. **Inset**. Zoom-in view of the $NiPS_3$ anisotropic exciton peak displaying peak DCP of 0.4. **lower panels**. S and P linearly polarized PL spectra acquired at different polarization detection angles indicated in the panels. All three spectra are excited by σ^+ polarized laser in the same way as the top panel. **b**. DLP of $NiPS_3$ anisotropic exciton (red data points and trace of **top panel**) and PL peak 1-3 (**lower panels**) as the function of polarization detection angle. Black data points and trace plot DLP of $NiPS_3$ anisotropic excitons in unstrained $NiPS_3$. **c**. Histogram of the linewidths of chiral quantum light emitters yielding 3.6 ± 1.3 meV average and standard deviation, respectively. ~40% of the QEs display linewidth narrower than 3 meV. We believe the linewidth can be further minimized via encapsulation in hBN. Both linewidth and chirality show no notable dependence on laser excitation power. **d**. Pump-dependent study of a nanoindentation with two circularly polarized PL peaks. **e, f**. The plot of DCP and linewidth as the function of the pump displays a little change over 3 orders of magnitude change in pump power. The DCP of peaks a & b is calculated by taking the rise of the un-polarized PL background into account.

Extended Data Fig. 6: Another Chiral Quantum Light Emitter showing -0.7 DCP and 96% single photon purity

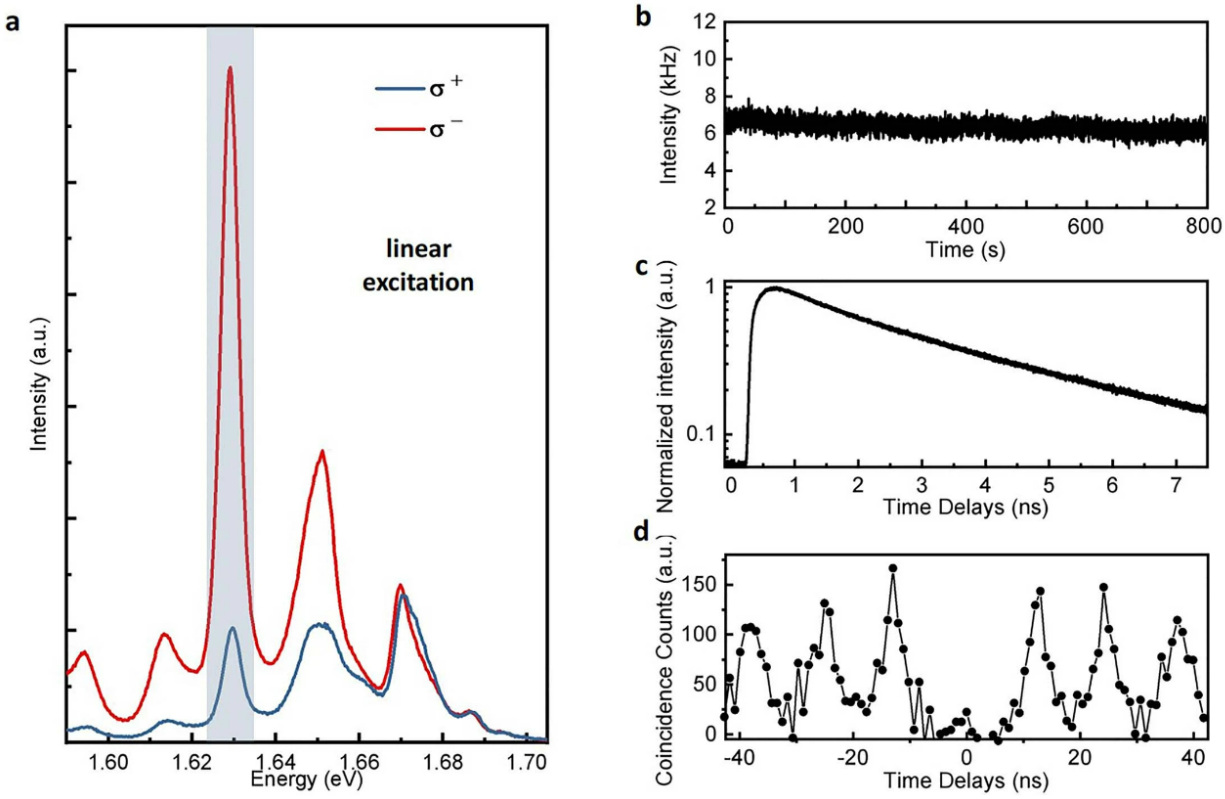

a. Chiral PL spectra (σ^+ (blue) and σ^- (red)) of another indentation spot under linearly polarized laser excitation showing >70% of DCP. **b**. PL intensity time trace, **c**. PL decay curve, **d**. 2nd order photon correlation trace collected at 10 K showing a $g^{(2)}(0) = 0.04$.

Extended Data Fig. 7: Room temperature (RT) scanning diamond NV microscopy study of indented $NiPS_3$

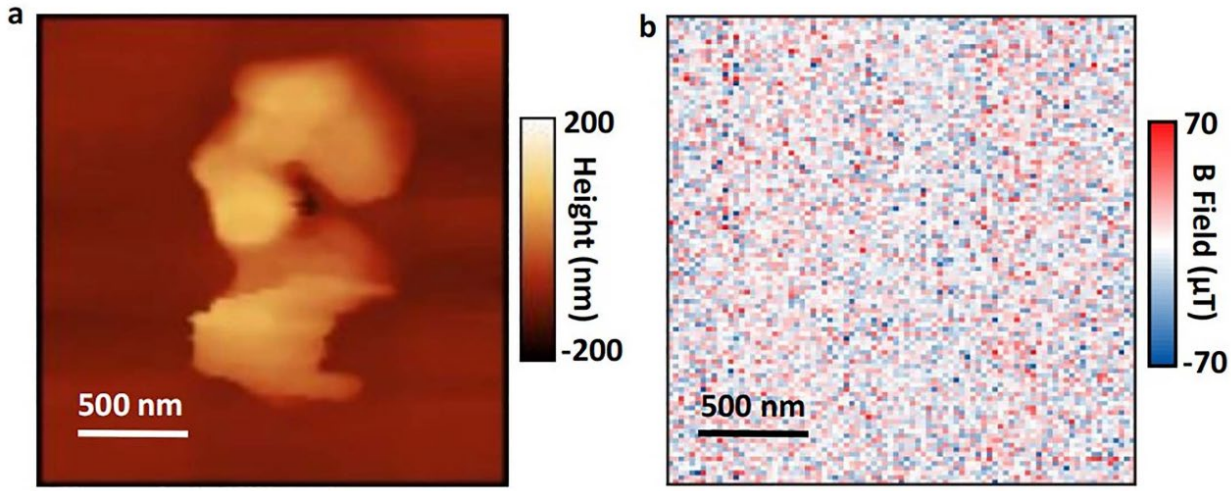

a. Topographical image of the indentation shown in Fig. 3c. The RT scanning NV system utilized a slightly sharper NV probe yielding a higher resolution topographical image. **b**. Magnetic field image of the same area showing only the noise.

Extended Data Fig. 8: Complete data set for Fig. 4a

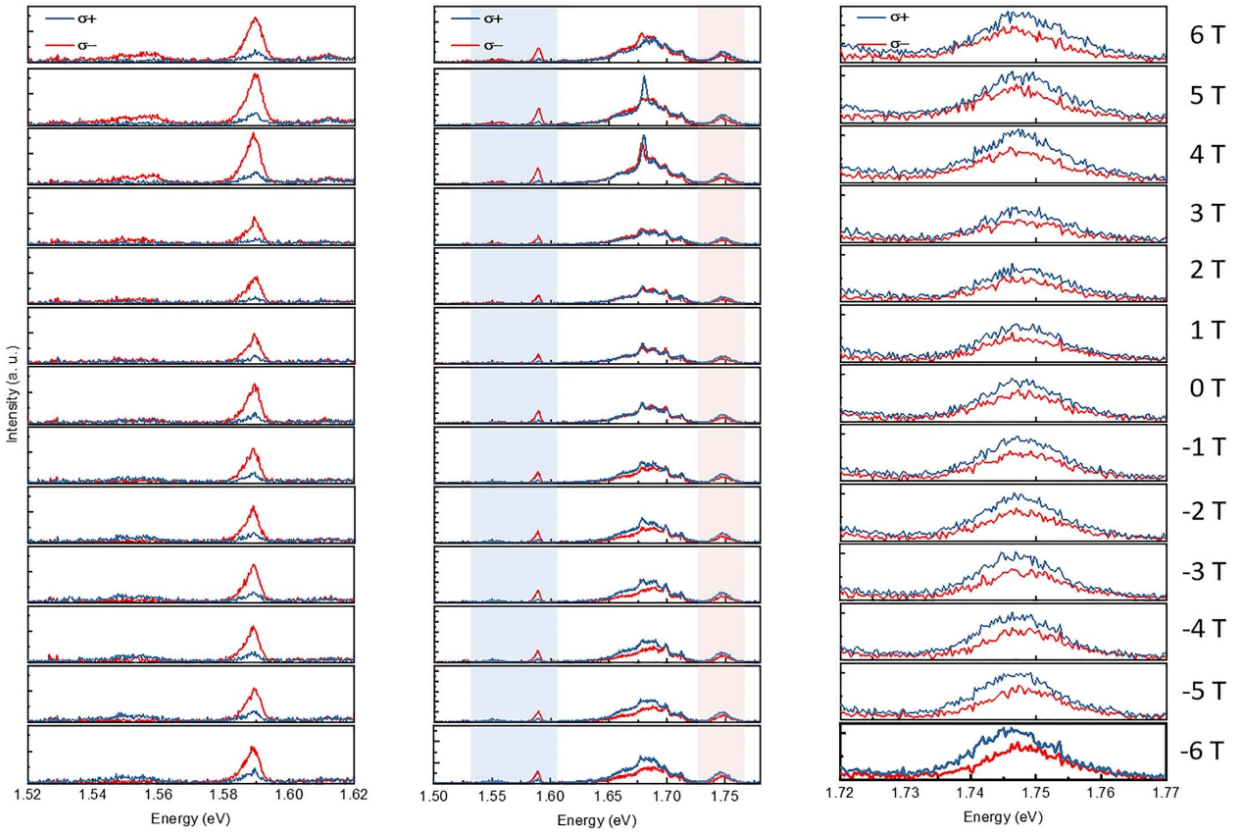

Center panel. Low-temperature σ^+ and σ^- polarized PL spectra acquired under -6.0 T to +6.0 T external magnetic field applied perpendicular to the sample plane. **Left and right panels**. Zoom-in view of the gray and red spectra ranges of the center panels. Because magneto-PL spectra were acquired under 633 nm σ^+ laser excitation, a weak DCP is observed at zero *B* field. A weak magnetic field-dependent change in DCP likely resulting from field-induced polarization of localized excitons is also observed in the 1.65 to 1.70 eV spectral range.

Extended Data Fig. 9: Complete data set for Figs. 4c and 4d

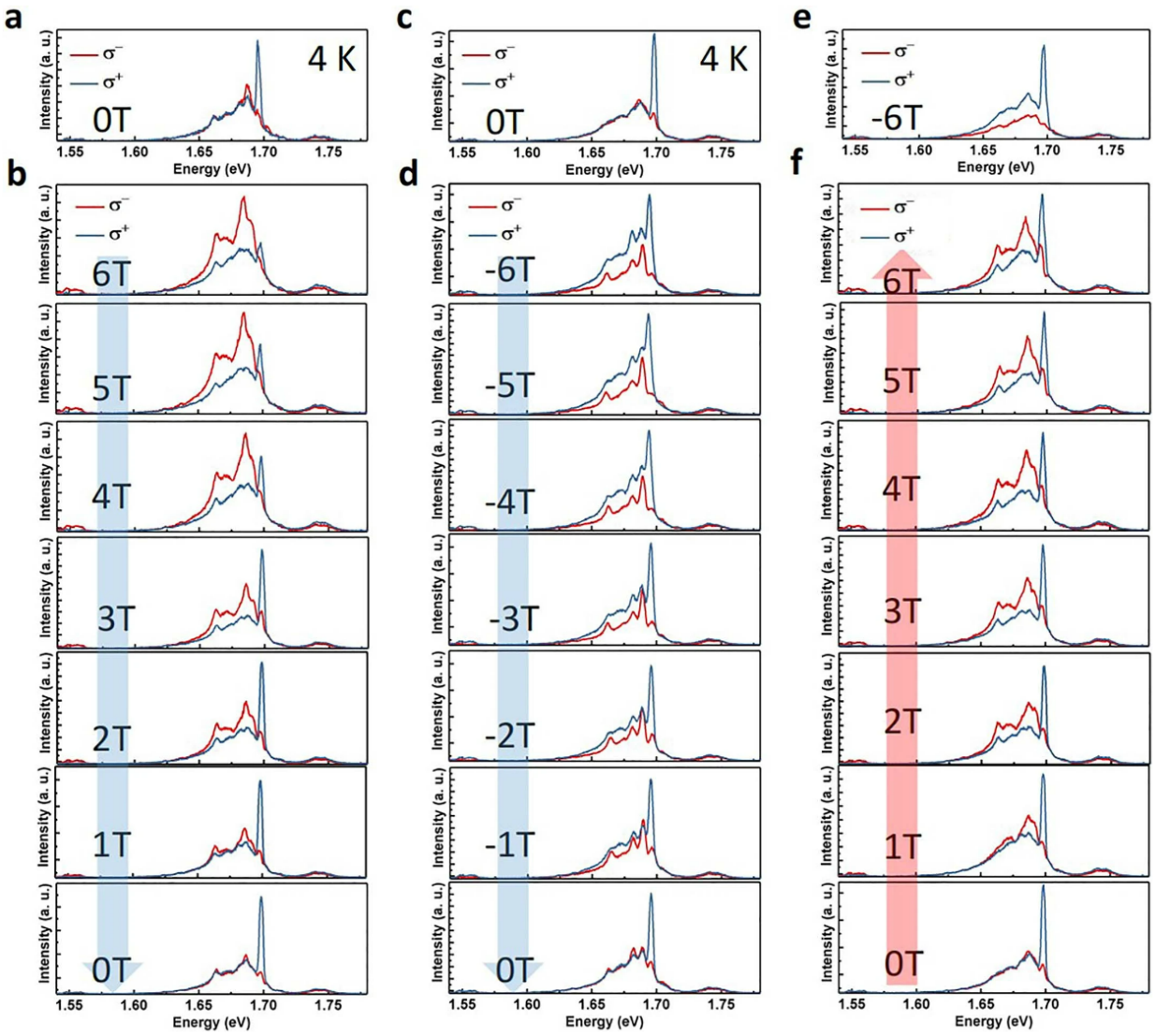

a-b, c-d. Complete B field dependent $\sigma^{+/-}$ polarized PL spectra shown in the bottom 3 panels of Fig. 4c and Fig. 4d. **e-f**. After chiral emission is fully restored at 0 T in b, PL spectra of the same location were collected by sweeping the field from 0 T to 6 T and then 6 T to -6 T.

Extended Data Fig. 10: Observation of Chiral Localized Exciton Emission from $WSe_2/FePS_3$ and $WSe_2/MnPS_3$ heterostructures with nano-indents

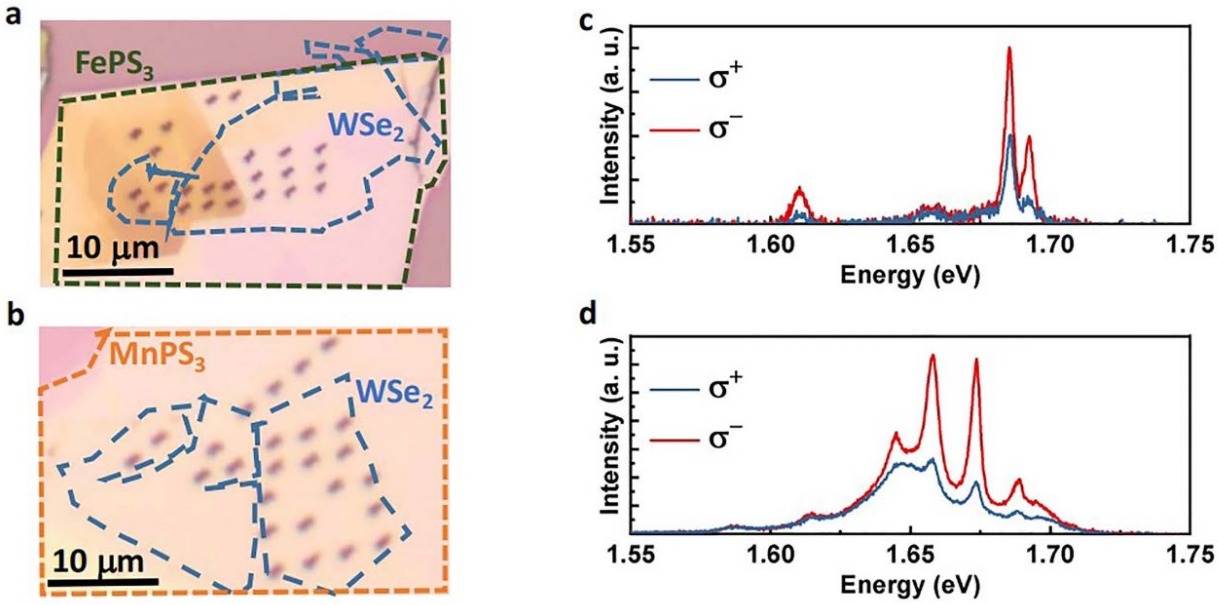

a-b. Optical images of the $WSe_2/FePS_3$ (a) and $WSe_2/MnPS_3$ (b) heterostructures with nano-indents. **c-d**. σ^+ and σ^- polarized PL spectra acquired under linearly polarized laser excitation at 4 K from two different nano-indents of $WSe_2/FePS_3$ (c) and $WSe_2/MnPS_3$ (d), respectively.

Supplementary Information

1. Competition between anisotropic exchange and Zeeman splitting

QEs resulted from localization of excitons are known to display anisotropic exchange splitting at zero field that leads to a pair of two orthogonal linearly polarized emission peaks as illustrated in Fig. S1, right panel. When the Zeeman splitting induced by the external B filed ($\mu_B g_{eff} B_z$) is much larger than the anisotropic exchange splitting (Δ_{XY}), the two fine structure state become circularly polarized. However, when $\hbar\mu_B g_{eff} B_z \sim \Delta_{XY}$, the lower and upper fine structure states will display only a partial circular polarization. In this case, as illustrated schematically in middle panel of Fig. S1, both lower and higher energy fine structure states will displays both σ^+ and σ^- polarized components due to partial linear polarization of the emission. Such B field dependent behavior has been observed originally in quantum dots [SR1]. Using effective pseudo-spin Hamiltonian approach Nestoklon et al.,[SR2] derived expression for the energy splitting and degree of circular polarization (DCP) of the fine structure as

$$\Delta = \sqrt{(\Delta_{XY})^2 + \left(\mu_B g_{eff} B_z\right)^2}, \tag{12}$$

$$DCP = \frac{\left(\mu_B g_{eff} B_z\right)^2}{(\Delta_{XY})^2 + \left(\mu_B g_{eff} B_z\right)^2}. \tag{13}$$

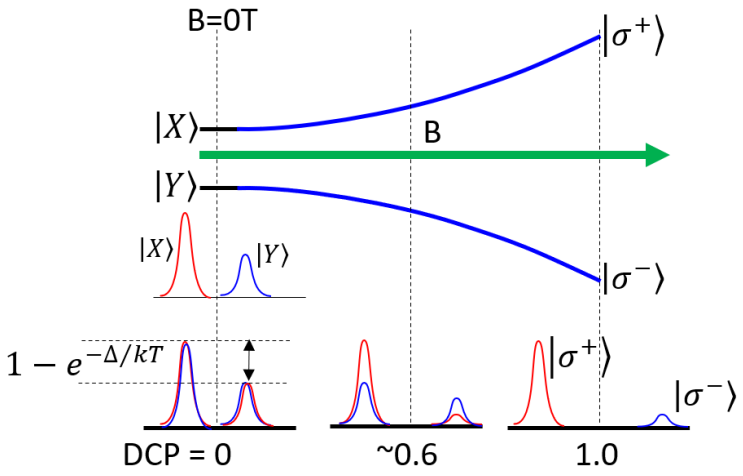

Fig. S1. Schematic illustration of anisotropic exchange and magnetic Zeeman interactions competing in defining the polarization of fine exciton spin doublet.

QEs of WSe_2 monolayer are also shown to display zero-field anisotropic exchange splitting of ~ 1 meV and a similar B field dependent behavior [SR3-5]. As anisotropic exchange splitting originates from the asymmetry of the strain induce confinement potential, our QE could also possess such fine structure splitting. Coupling to the $NiPS_3$ could further enhance the anisotropic exchange interaction.

We postulate that this anisotropic exchange splitting can compete with valley splitting induced via magnetic exchange interaction with AFM defect of $NiPS_3$ in a similar manner as in case of external B field induced Zeeman splitting. This competition will results in two fine structure states displaying partial circular polarization (Fig. S1 middle panel) at zero B-filed. The higher energy peak, on the other hand, could become undetectable since their intensities will be reduced by Boltzmann factor of $Exp(-\Delta/k_BT)$.

References:

SR1. H. Htoon, S. A. Crooker, M. Furis, S. Jeong, A. L. Efros, V. I. Klimov, Anomalous circular polarization of photoluminescence spectra of individual CdSe nanocrystals in an applied magnetic field, Phys. Rev. Lett. **102**, 017402, (2009).

SR2. M. O. Nestoklon, S. V. Goupalov, R. I. Dzhioev, O. S. Ken, V. L. Korenev, Yu. G. Kusrayev, V. F. Sapega, C. de Weerd, L. Gomez, T. Gregorkiewicz, Junhao Lin, Kazutomo Suenaga, Yasufumi Fujiwara, L. B. Matyushkin, and I. N. Yassievich, Optical orientation and alignment of excitons in ensembles of inorganic perovskite nanocrystals, Phys. Rev. B, **97**, 235304 (2018)

SR3. A. Srivastava, M. Sidler, A. V. Allain, D. S. Lembke, A. Kis, A. Imamoğlu, A, Optically active quantum dots in monolayer WSe_2. Nat. Nanotechnol. **10**, 491 (2015)

SR4. Y. -M. He, G. Clark, J. R. Schaibley, Y. He, M. -C. Chen, Y. -J. Wei, X. Ding, Q. Zhang, W. Yao, X. Xu, Single quantum emitters in monolayer semiconductors. Nat. Nanotechnol. **10**, 497-502, (2015).

SR5. K. Shayan, N. Liu, A. Cupo, Y. Ma, Y. Luo, V. Meunier, S. Strauf, Magnetic proximity coupling of quantum emitters in WSe_2 to van der Waals ferromagnets, *Nano Lett.,* **19**, 7301 (2019);